OPEN ACCESS
IOP Publishing
Semiconductor Science and Technology
Semicond. Sci. Technol. **39** (2024) 085001 (10pp)
https://doi.org/10.1088/1361-6641/ad575b

Microscopy studies of InGaN MQWs overgrown on porosified InGaN superlattice pseudo-substrates

Yihong Ji[1,*], Martin Frentrup[1], Simon M Fairclough[1], Yingjun Liu[2], Tongtong Zhu[2] and Rachel A Oliver[1,2]

[1] Department of Materials Science and Metallurgy, University of Cambridge, Cambridge, United Kingdom
[2] Poro Technologies Ltd, Sawston, Cambridge, United Kingdom

E-mail: yj335@cam.ac.uk

Received 12 February 2024, revised 15 May 2024
Accepted for publication 12 June 2024
Published 24 June 2024

Abstract

In this study, possible origins of small V-pits observed in multiple quantum wells (MQWs) overgrown on as-grown and porosified InGaN superlattice (SL) pseudo-substrates have been investigated. Various cross-sectional transmission microscopy techniques revealed that some of the small V-pits arise from the intersection of threading defects with the sample surface, either as part of dislocation loops or trench defects. Some small V-pits without threading defects are also observed. Energy dispersive x-ray study indicates that the Indium content in the MQWs increases with the averaged porosity of the underlying template, which may either be attributed to a reduced compositional pulling effect or the low thermal conductivity of the porous layer. Furthermore, the porous structure inhibits the glide or extension of the misfit dislocations (MD) within the InGaN SL. The extra strain induced by the higher Indium content and the hindered movement of the MDs combined may explain the observed additional small V-pits present on the MQWs overgrown on the more relaxed templates.

Keywords: InGaN, MQWs, V-pits, microLED, porosification, TEM

1. Introduction

Indium gallium nitride (InGaN), being a direct bandgap III–V semiconductor material, has attracted extensive interest in academic and industrial research due to its high potential for next-generation display technology applications, including ultra-large and very small high-resolution displays, augmented reality (AR) and virtual reality (VR) [1–3]. Compared to other materials, InGaN allows the use of the same materials system for blue, green and red LEDs whilst the efficiency of nitride LEDs is less affected by miniaturization to the micron-scale than devices based on materials like AlInGaP [4]. However, unlike other III–V materials, wurtzite InGaN suffers from inherent spontaneous polarization. Furthermore, strong strain-related piezoelectric polarization fields arise along the *c*-direction [0001] in heterostructures, caused by the large lattice mismatch between InGaN and GaN [5]. These polarization fields lead to a reduced overlap of the electron and hole wavefunctions in quantum wells and hence a reduced radiative recombination rate, allowing non-radiative recombination processes to become competitive, and hence reducing efficiency. This so-called quantum confined Stark effect (QCSE) is especially detrimental to the efficiency of long wavelength InGaN-based μ-LEDs, as high InN contents are required to achieve red, amber and green emission [6]. Furthermore, the stress in compressively strained InGaN layers hampers the incorporation efficiency of In during the epitaxial growth of the

* Author to whom any correspondence should be addressed.

LED heterostructure, which makes achieving long-wavelength emission more difficult [7]. Strain can also lead to the incorporation of additional extended defects [8], leading to increased non-radiative recombination rates.

Flexible, partially relaxed porous InGaN pseudo-substrates with lattice parameters closer to that of the multiple quantum wells (MQWs) active region of the LEDs can potentially provide a route to overcome these strain-related issues [9]. Several approaches to porosify GaN-based templates have been demonstrated in the literature, but many of these techniques relax areas of limited size in the order of a few tens of microns and/or require multiple elaborate processing steps [10, 11]. In our previous study [12], a defect-mediated electrochemical etching (ECE) method was adopted to porosify an InGaN superlattice (SL) at the wafer scale without the need for additional costly patterning. We showed that porosification of the SL could be achieved without causing any substantial change to the sample surface, allowing the porosified InGaN SL structures to be used as a pseudo-substrate for the overgrowth of InGaN MQWs. We demonstrated that a substantial strain relaxation of the InGaN SL and MQWs of up to ca. 45% can be achieved by engineering the porosity in the porous SL template through appropriate control of the etching voltage. However, in addition to the strain relaxation, newly formed small V-pits present on the InGaN MQWs surface were observed, which increased in density and size with increasing etching voltage [12]. As these small V-pits might be related to defects newly formed in the MQW structures and might offer a potential route for plastic relaxation, it appears contradictory that the highest density of small V-pits has been observed in the most porosified and most relaxed sample.

In this paper, we explore the origin of these V-pits and their role in strain relaxation using transmission electron microscopy (TEM). We show that small V-pits formed in MQWs overgrown on porous InGaN pseudo-substrates can arise either at the termination of threading dislocations (TDs) associated with misfit dislocations (MDs) or in relation to sub-surface basal plane stacking faults (BSFs). We further show that increasing the porosity of the porous layers leads to an increase in the indium content of the MQW structure and discuss the impact of both the change in porosity and the composition on the subsequent strain relaxation.

2. Sample details and methods

The samples investigated here were provided by Poro Technologies Ltd (Porotech) and consist of InGaN-based pseudo-substrates, which were porosified by ECE prior to the overgrowth with InGaN MQWs. Figure 1 illustrates the sample structure. The pseudo-substrates were grown on 2-inch sapphire substrates and consisted of a 2 μm-thick GaN buffer layer, a 250 nm thick layer of nominally undoped GaN (uid-GaN), followed by ten pairs of 20 nm-thick unintentionally doped $In_{0.09}Ga_{0.91}N$ (uid-InGaN) and highly Si n-doped $In_{0.06}Ga_{0.94}N$ (n-InGaN) layers ($n_{Si} = 1 \times 10^{19}$ cm^{-3}). This SL was capped with a 20 nm-thick layer of uid-$In_{0.12}Ga_{0.88}N$.

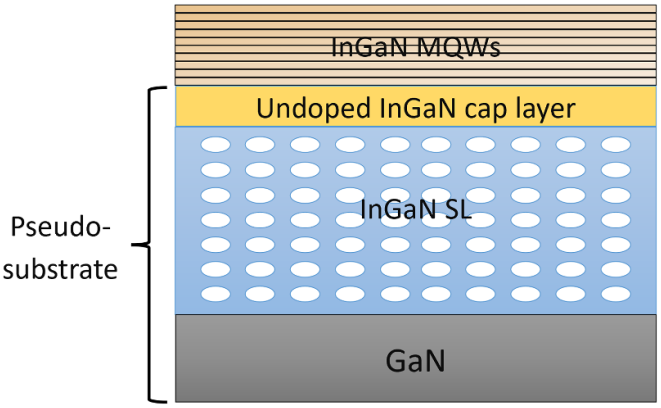

Figure 1. Schematic structure illustration of the InGaN MQWs overgrown on a porosified SL template.

A further five pairs of nominally 7 nm-thick $In_{0.06}Ga_{0.94}N$ quantum barriers (QBs) and 3 nm-thick $In_{0.1}Ga_{0.9}N$ QWs were overgrown on two different templates that were etched under voltages of greater than 6 V to achieve porosification. Details of the etching process and the structural and morphological characterization of the porous pseudo-substrates can be found in [12]. In order to maintain consistency and for the convenience of cross-referencing, samples used in this study are labeled in the same way as in our previous publication [12] as sample B2 (medium etched) and sample B3 (most etched). The edge of each sample wafer has intentionally remained unetched as a comparator for the adjacent porosified material.

In order to study the V-pits and associated defect structure in these samples, several cross-sectional lamellae were prepared in a field electron and ion (FEI) Helios dual-beam nanolab focused ion beam (FIB) microscope. Standard sample preparation techniques were applied using Pt as the coating layer, 30 kV Ga^{3+} ion beam for initial milling and 5 kV Ga^{3+} ion beam for the final polish. Two cross-sectional lamellae with a thickness of less than 60 nm from the non-porous region of the medium-etched sample B2 were prepared. Lamellae with a thickness of about 100 nm from the porous region of each of the samples were also prepared. For energy-dispersive x-ray (EDX) analysis (see below), all samples were placed on the same TEM grid.

To facilitate the visualization and identification of subsurface structural defects in the samples, a series of weak beam dark field (WBDF) images under 3 g-excitation conditions were collected in a FEI Tecnai Osiris TEM operated at 200 kV. Scanning transmission electron microscopy (STEM) studies were conducted in a Thermo Fisher Scientific^{TM} Spectra 300 operated at 300 kV with a convergence angle of about 23 mrad and equipped with four Super-X detectors. A segmented annular dark field (ADF) detector with two rings for collection at an angle between 24 mrad to 48 mrad (inner ring) and an angle between 48 mrad to 90 mrad (outer ring), referred to as DF-I and DF-O respectively, was used to locate potential defects in the samples. A high-angle ADF (HAADF) detector with a collection angle between 101 mrad and 200 mrad was used for z-contrast imaging of these defects with atomic-level

resolution. To maximize the ADF and HAADF image quality, a beam current of about 30 pA was used. Elemental mapping of the InGaN MQWs above the porous SLs was carried out using EDX in the STEM with a beam current between 140 pA and 150 pA. From each lamella three different EDX profiles with a step size of 0.65 nm and integrated over a width of about 38 nm were collected. The regions for the EDX analysis were chosen so that they are at least 1 μm apart from each other and do not overlap with the sidewalls of V-pits and other structural inhomogeneities at which the local composition might vary due to differences in the incorporation efficiency. As the specimens of the porous samples were mounted on the same TEM grid, the elemental analyzes were done in succession without changing the sample holder. The holder was an FEI-clipped low-profile double tilt holder.

3. Results and analysis

3.1. Routes for the formation of small V-pits

First, we will investigate the sub-surface defect structure associated with V-pits in the samples, for which WBDF imaging has been employed. As the strain in and above the porosified regions of the SLs may be inhomogeneous, which could lead to unwanted variations in the diffraction contrast, a non-porosified reference region from the edge of sample B2 with homogenous in-plane strain, has been chosen for the initial WBDF examination. Figure 2(a) shows such a WBDF image collected under the 3 g-excitation condition with $g = 1\bar{1}00$ (see figure 2(b)), for which the sample was tilted so that the 3 g spot satisfies the Bragg condition. In the image, sharp interfaces may be observed between the thick GaN buffer layer and the individual InGaN SL layers as is visible by the bright-dark contrast between the layers. In the top part of the WBDF image, figure 2(a), the InGaN cap layer and InGaN MQWs are less distinguishable from each other due to their small thickness and similar composition. Therefore, the labeling of these layers is based on the 200 nm scale bar and the known structure. TDs present in the underlying GaN buffer layer (labeled as 1) arise from the GaN/sapphire interface. When these TDs reach an interface, they either extend straight towards the surface (1_A), opening up to large V-pits or bend at the interface (1_B).

Figure 2(a) also shows small V-pits at the sample surface, with threading defects beneath them (labeled as 2). As the (degree of) porosification mainly influences the density and distribution of small V-pits [12], we will focus on the sub-surface structure related to the small V-pits. We will start our examination with the non-porous region of sample B2 and will later also address small V-pits in the MQWs above the porosified regions of the different templates. Figures 2(c)–(f) show magnified images of the four regions I, II, III and IV, marked in the overview image (figure 2(a)). As can be seen from these zoomed-in images, the small V-pits (indicated by white arrows) are very shallow, and their apex is located within the QWs near the surface. Furthermore, each of the small V-pit is connected to a threading defect beneath it (indicated by the yellow arrows), which further penetrates into the InGaN SL. Although some of the threading defects penetrate into the SL, this does not necessarily imply that the defects were present during the growth of the SL. If the threading defects were present during the growth of the SL, we might expect to see changes in the thickness or orientation of the SL layers related to the presence of the defect during the growth. No such changes are observed. In general, surface V-pits form during InGaN growth either part of a dislocation loop (consisting of one MD and two TDs) [13] or part of a trench defect (consisting of a BSF and a stacking mismatch boundary (SMB) enclosing a volume of QW material) [14] due to the large lattice mismatch and the related strain. For dislocation loops, dislocations may glide down into the SL during QW overgrowth whilst simultaneously the threading components open up into small V-pits at the surface. Holec *et al* used TEM to verify this dislocation glide phenomenon in MQWs [15] whilst El-Ella *et al* provided evidence that this also applies in SLs [16].

Based on the evidence presented so far in figure 2, it is not clear whether the defects seen here relate to dislocation loops or trench defects. In addition to the threading defects, one can also observe in figure 2 in-plane defects marked by the blue arrows. By analyzing these in-plane defects, we hope to shed light on the nature of the threading defects and the origin of the small V-pits.

To identify the type of in-plane defect shown in figure 2, a series of WBDF images were collected for region IV at different (α, β) tilting angles, where the high tilt is approximately (15°, 7°) away from the low tilt condition. In the low-tilt image in figure 3(a), a small surface V-pit within the InGaN MQWs is seen connected to a threading defect that penetrates into InGaN SL. The bottom of the threading defect is attached to an in-plane defect. Under low tilt conditions in figure 3(a) this in-plane defect is visible as a dark horizontal line with a narrow width (indicated by the blue lines). When the lamella is tilted to higher angles in figure 3(b) this horizontal line increases in width and shows a characteristic black/white/black contrast. These two changes suggest that this in-plane defect may be a planar defect within the interface, likely a BSF. To further confirm this assumption, a series of atomically resolved HAADF STEM images were collected from the region where the threading defect and the in-plane defect intersect with each other as indicated by the yellow box in figure 3(b)). Figure 3(e) shows an atomically resolved HAADF STEM image recorded near the interface between the last InGaN SL layer and the cap layer. It reveals that the stacking order of the close-packed (0002) planes changes from …ABABAB… to …BCBCBC… at the specific position indicated by the white arrow. This change in stacking is a characteristic of I_1-type stacking faults, which are the most common stacking faults found in wurtzite GaN with the lowest formation energy among the variant types of stacking faults [17]. It is therefore reasonable to conclude that the small V-pit shown in figures 3(a) and (b) is part of a trench defect, and the threading defect is an associated SMB.

However, not all of the small V-pits and threading defects are associated with trench defects as the following analyzes will show. A typical characteristic of an SMB is that it starts

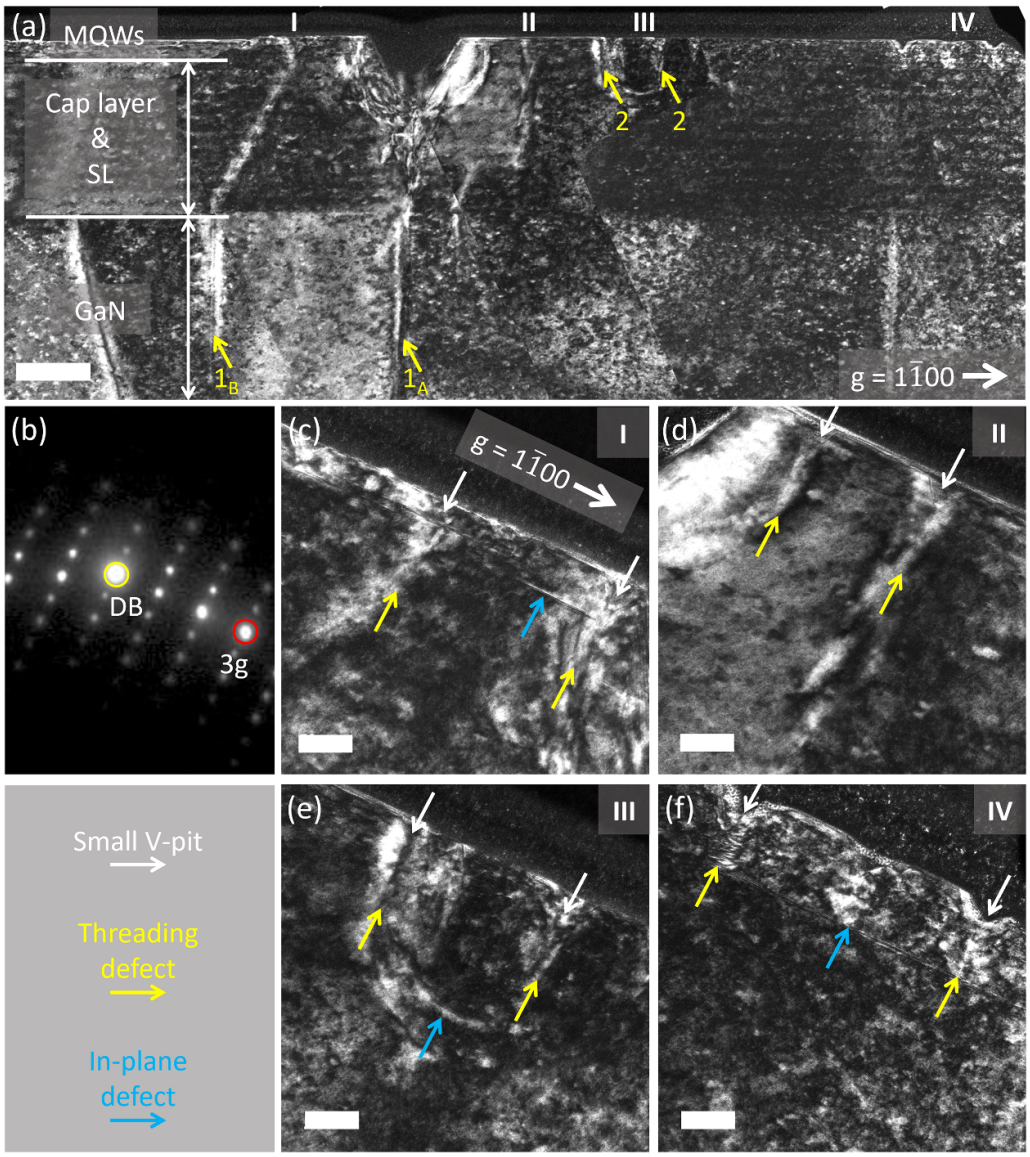

Figure 2. (a) WBDF image taken along the [11$\bar{2}$0] zone axis (with $g = 1\bar{1}00$) of the non-porous region of sample B2. (b) Recorded selected-area diffraction pattern where the direct beam (DB) and the 3 g diffraction disc are highlighted. (c)–(f) Magnified images of regions I, II, III, and IV respectively. The scale bars are (a) 200 nm and (c)–(f) 50 nm, respectively.

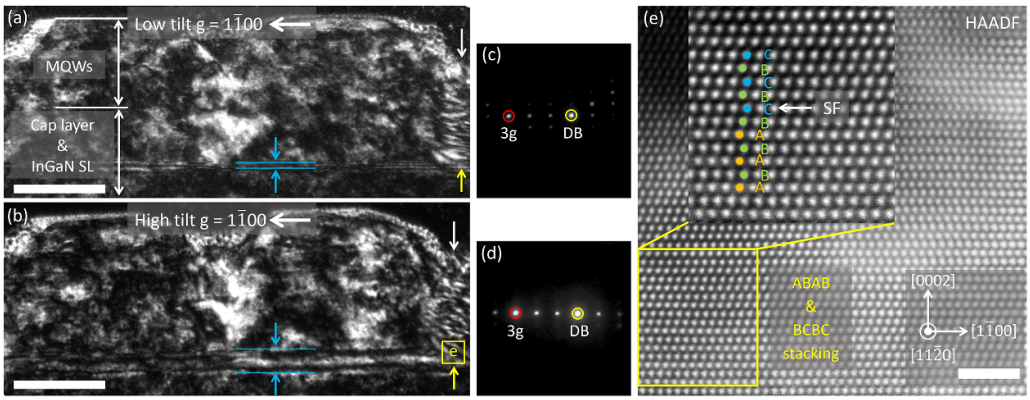

Figure 3. WBDF images taken along [11$\bar{2}$0] zone axis (with $g = 1\bar{1}00$) of Region IV shown in figure 2(f) observed under (a) low tilt and (b) high tilt conditions, and their corresponding recorded diffraction pattern are shown in (c) and (d) respectively. (e) Atomically resolved HAADF STEM image taken along the [11$\bar{2}$0] zone axis of the area highlighted by the yellow square in (b) revealing a type I_1 BSF. The scale bars are (a), (b) 50 nm and (e) 2 nm, respectively.

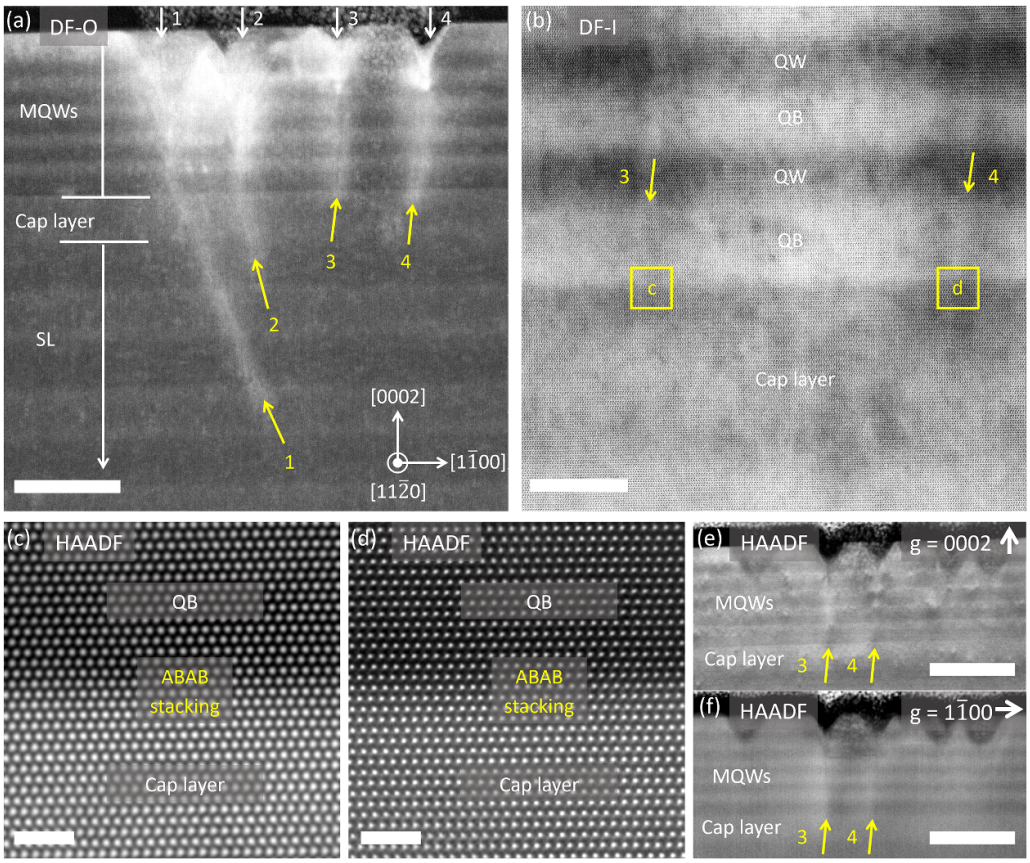

Figure 4. STEM images of the non-porous region in sample B2 recorded in (a) DF-O detector and (b) DF-I detector. (c), (d) Atomically resolved HAADF image taken along the [11$\bar{2}$0] zone axis of the areas marked by yellow squares in (b). (e), (f) HAADF images collected in 2-beam condition with $g = 0002$ and $1\bar{1}00$ respectively. The scale bars are (a) 50 nm, (b) 10 nm, (c), (d) 2 nm and (e), (f) 50 nm, respectively.

from the edge of a SF and runs perpendicularly to the c-plane all the way to the apex of the surface V-pit [18]. For better visualizing the orientation of the sub-surface defects, ADF STEM was employed on a second lamella prepared from the non-porous region of sample B2. This method is sensitive to the diffraction contrast caused by defects [19]. The DF-O STEM image of the non-porous region in figure 4(a) shows four small V-pits at the surface confined within the topmost three sets of QWs. The four corresponding threading defects ending at the apex of each small V-pit propagate into the cap layer or extend even further below into the InGaN SL (TD 1 and 2). Interestingly, these four threading defects are not normal to the (0002) planes, but are all slightly inclined, and threading defects 1 and 2 even bent when they entered the InGaN SL. Figure 4(b) shows a high-magnification DF-I STEM image of the threading defects 3 and 4 near the interface between the MQWs and the cap layer. Both defects appear to end at the interface to the cap layer and there is no obvious sign of an in-plane defect that connects the ends of these two threading defects. Atomically resolved HAADF STEM images were taken from the interface between the cap layer and the first QB exactly below both threading defects, at the locations indicated by both yellow boxes. The corresponding images in figures 4(c) and (d) show that the stacking sequence of the (0002) planes within the imaged area remains the characteristic …ABABAB… order without any stacking error being visible. This confirms the absence of a stacking fault between both defects, suggesting that threading defects 3 and 4 are not SMBs. A further analysis by HAADF STEM imaging under two-beam condition at $g = 0002$ and $g = 1\bar{1}00$ show a faint contrast in both images figures 4(e) and (f) respectively. This observation together with the absence of any planar defects nearby suggest that the threading defects are mixed-type TDs, and the two corresponding small V-pits are part of the same or a different dislocation loop. In this context it should be noted that for a dislocation loop, the contrast of the in-plane MD may not be visible (see figure 4(a)) due to the FIB preparation or the relative orientation between MD and TEM imaging direction. Alternatively, if the TDs are inclined, then TDs may intersect the side of the TEM lamella, and hence the related MD would not be in the sample but would have been removed during sample preparation. However, this explanation would not be consistent with the typical structure of a trench defect, and so only backs up the suggestion that these threading defects are just TDs. Furthermore, the lack of bending of the SL layers, suggests that this is a defect formed during overgrowth; however, we are aware of no feasible mechanism by which a BSF could move down from the QWs into the SL during overgrowth. Again, this supports the assignment of these defects as part of a dislocation loop.

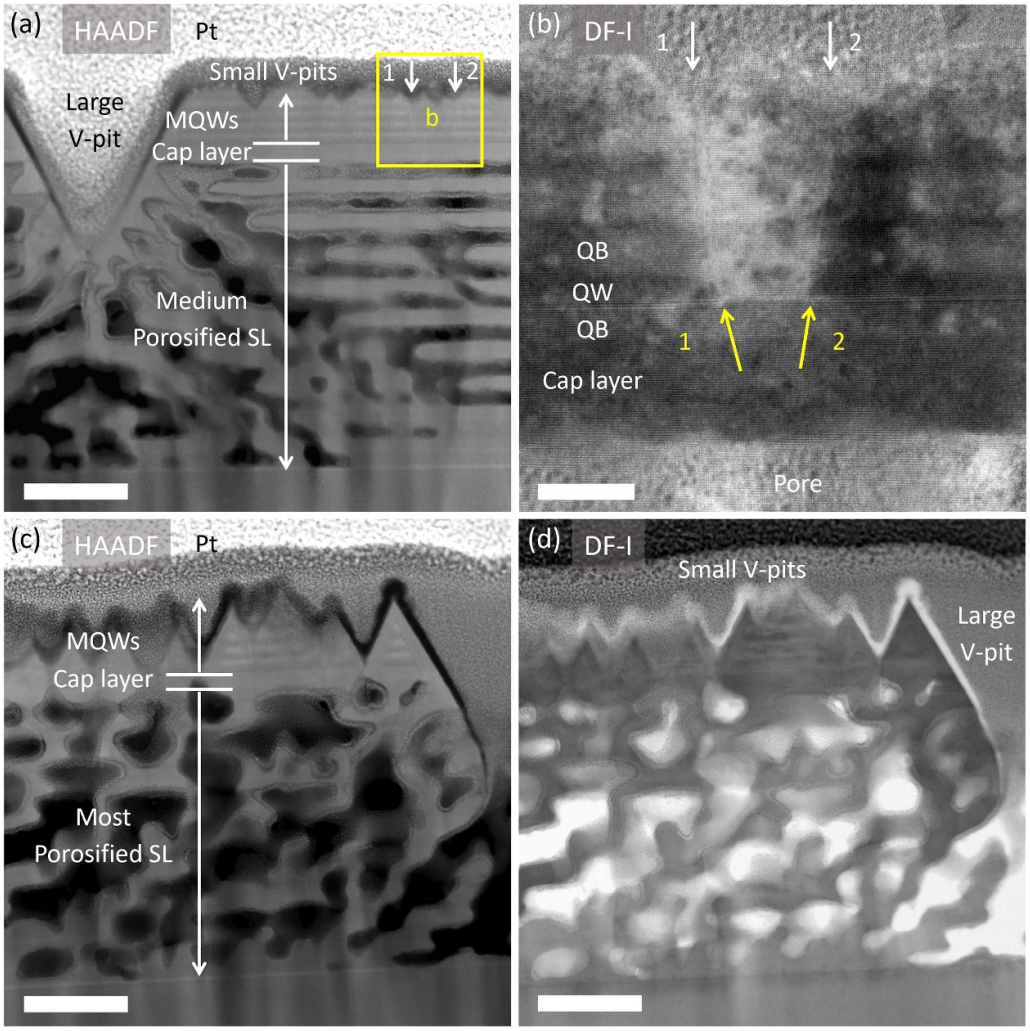

Figure 5. STEM images of the porous region in sample B2 (top row) and sample B3 (bottom row) recorded in (a), (c) HAADF and (b), (d) with a DF-I detector respectively. The scale bars are 100 nm for (a), (c), (d) and 20 nm for (b).

We will now draw our attention to the defect structure associated with small V-pits above the porosified SL layers. TEM imaging of these specimens is especially challenging, as local variations of the strain caused by the alternation of pores and remaining material lead to strong inhomogeneous strain contrast. Furthermore, the higher flexibility of the porous structure (desired for the strain relaxation of the template) makes the TEM lamella more fragile and susceptible to bending. Both, the inhomogeneous strain contrast and the bending of the lamellae, lead to artifactual intensity variations heavily superimposing upon the contrast from the defects.

Figure 5(a) shows a cross-sectional HAADF STEM image of the medium-etched sample B2, in which alternating porous and non-porous layers in the InGaN SL are clearly visible. These pores are formed by ECE, during which the etching solvent reaches and etches the subsurface n-doped InGaN layers through TDs acting as nanopipes [20]. Whilst a large V-pit exists a high number of small V-pits penetrating the three topmost QWs can be seen throughout the surface, similar to those previously observed for the non-porous region of this sample (e.g. in figures 3 and 4) but in higher density as also previously confirmed by AFM measurements [12]. A high-magnification DF-I STEM image of two of these small V-pits in figure 5(b) reveals that the threading defects marked by arrows 1 and 2 are present at the apexes of these newly formed small V-pits, which further reach down to near the interface between the 1st QB and QW where the overgrowth started. Whilst challenging to image, the presence of these threading defects and the fact that they stop either at the interfaces within the MQWs or between the MQWs and the cap layer suggest that they are very likely of the same nature as the threading defects seen in the non-porous region—namely TDs as part of dislocation loops and SMBs as part of trench defects.

It should be noted that many small V-pits are penetrating the MQWs in this lamella (not shown here) where we have been unable to identify any threading defects beneath them. It is possible that the threading defects below these V-pits were cut off during FIB sample preparation. Given that the number of these V-pits without associated threading defects is relatively high and not even small threading segments could be identified makes it more likely that the apexes of these small V-pits directly connect to an in-plane defect or that these small V-pits

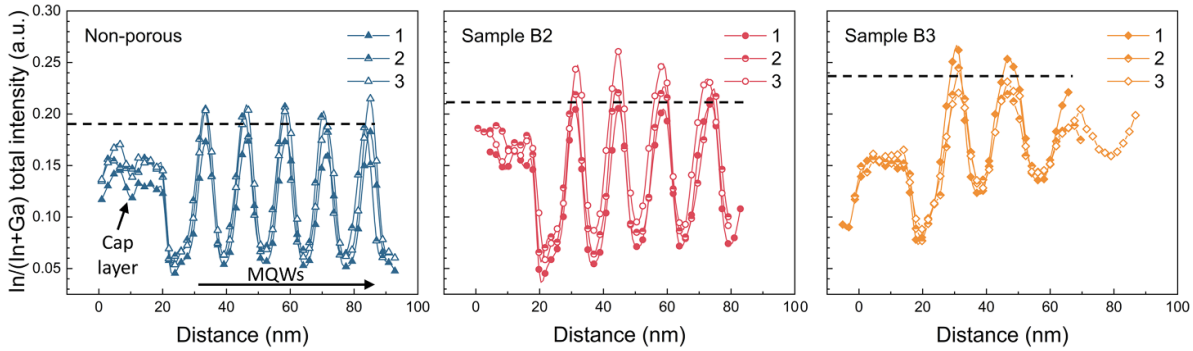

Figure 6. EDX quantification of In/(In + Ga) total intensity for the cap layer and MQWs of the non-porous reference sample, and the porosified regions of sample B2 and sample B3 (from left to right). The dashed line indicates the approximate In content across the MQWs for each sample.

in and of themselves represent a strain relaxation mechanism. This hypothesis is also supported by STEM images of the porous region of the most etched sample B3 in figures 5(c) and (d). The images show an extremely high density of small V-pits penetrating through all or nearly all the QWs to the interface between MQWs and cap layer without any clear evidence for the presence of threading defects, suggesting that the V-pits open up straight away upon growth of the first QB.

3.2. Source of extra strain related to the increased small V-pits

The previous section revealed that there are three possible routes for the formation of small V-pits newly formed within MQWs: (a) be part of trench defects which consist of one basal plane SF with vertical SMBs, (b) of a dislocation loop which consists of one MD at the interface between two materials with different lattice constant and two TDs on either end of the MD segment. (c) V-pits nucleate without the presence of threading defects.

Whilst all these routes above serve to relax strain in the heterostructure, the combined increase in density of small V-pits and increase in average relaxation of the heterostructure as the porosity increases in our samples (see [12]) may therefore suggest the presence of another strain source. Given that no significant surface morphology change was observed for the InGaN SL after porosification and prior to the MQW overgrowth [12], a further mechanism could be a variation in the In composition of the InGaN MQWs structure among the samples.

Figure 6 shows a quantitative EDX analysis of the relative In content across the MQWs (normalized to the total group-III content (Ga + In)) for the non-porous region of sample B2 and the porosified regions of both samples B2 and B3. For each sample, compositional profiles from three different regions of each TEM lamella were recorded to increase the reliability of the measurement. Each profile was collected at a sufficient distance from the V-pits sidewalls (or other structural inhomogeneities) to avoid any impact of compositional variations at these features on the measurement. All three samples show clear oscillations of the In-content across the MQWs region as one goes from one QB to the QW and the next QB. Although all the MQWs were grown under nominally identical conditions, they exhibit strong differences in the In incorporation. The In content in the non-porous sample remains low and constant compared with the other two porosified samples, which is expected as the InGaN MQWs overgrown on the as-grown (non-etched) template are fully strained as confirmed by x-ray diffraction analysis [12]. As for the porous counterparts, they exhibit a significantly higher In content that increases with the porosity. However, the In incorporation in the MQWs of these two porosified samples is not constant but steadily increases along the growth direction, especially for the QBs. This can be attributed to increased strain relaxation with the formation of the small V-pits and related crystallographic defects, where present. Furthermore, we observed only small differences between the three EDX profiles of each sample, which suggest that the lateral, local (few micron scale) compositional variations are in the few percent range.

Quantitively, we note that the maximum In content of the QWs increases from about 19% for the non-porous sample to up about 24% for sample B3 as indicated by the dashed lines in figure 6. This could potentially be explained by the differences in the porosity of the underlying SL templates. If relaxation increases as porosity increases (which would be a reasonable inference from our previous work [12]), then the QWs grown on the most porosified template are also grown on the most relaxed surface, and this will lead to an increased In incorporation, due to a reduction in compositional pulling effect [21]. Another reason for the increase In incorporation could be related to the higher porosity directly. The porous SL might have a lower thermal conductivity [22] than its non-porosified counterparts. As these pseudo-substrates are heated from the backside during the growth process, the effective temperature at the surface where the MQWs grow is likely to be lower. Such a reduction in surface temperature at the growth front would also be expected [23] to lead to higher incorporation efficiency of In into the layers.

However, if the In content of the MQWs is higher on the more relaxed porous pseudo-substrate, this would imply that the actual driving force for relaxation in the MQWs is not reduced and may even increase. This could explain the increase in density of small V-pits on the more porosified

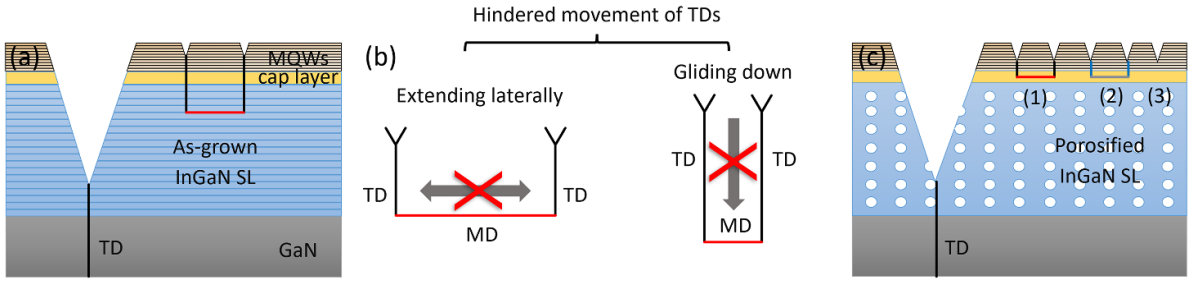

Figure 7. Schematic illustration of the formation mechanism of increased small V-pits with etching voltage. (a) A low density of small V-pits forms on the surface with wide and deep misfit segments. (b) The movement of the newly formed TDs during MQWs growth are hindered after porosification. (c) More small V-pits either as a part of (1) dislocation loops (2) trench defects or just (3) by themselves formed on the surface of the MQWs grown on porosified InGaN SL template. Note that the position of in-plane defects in (1) and (2) only serves as a reference, which does not represent the actual place.

templates as we observed. Overall, these data are consistent with strain relaxation in the overgrowth of porosified samples being due to both the relaxation of the underlying porous SL and also the formation of V-pits and related sub-surface defects.

4. Discussion

The electron microscopy study of the MQWs structures overgrown on fully strained and partially relaxed InGaN SL pseudo-substrates with different porosity has revealed the formation of a high density of newly formed small V-pits with increasing porosity and strain relaxation in the templates. We also observed higher In incorporation in the MQWs for larger template relaxations and porosities of the pseudo-substrates. This may have led to a stronger driving force towards strain relaxation via newly formed dislocation loops and stacking faults, and the opening of small V-pits associated with them. However, given that the observed change in indium composition is only up about 5%, this may not be a sufficient explanation for the strong change in the defect morphology across the samples. Other impacts of the porous structure of the template may also need to be considered.

Figure 7(a) illustrates the situation for MQWs grown on a non-porosified InGaN SL templates, where large V-pits open up from TDs formed further down in the template and small V-pits opened up at newly formed threading defects, for example as part of dislocation loops. These dislocation loops formed during the growth when the stored strain energy exceeds the limit at which it becomes energetically more favorable to form a MD in the growth plane which is connected to two TDs which extend to the surface. These dislocation loops can then glide further down into the SL or extend laterally to form a longer misfit segment to increase the strain relaxation. However, the situation is different for the SL templates after porosification as illustrated in figure 7(b). The pores within the SL structure will prevent the glide of the dislocation loops further down into the structure. Furthermore, local strain variations relating to the inhomogeneities in the porous structure and potentially to small local compositional variations in the low 1% range will hinder the lateral extension of the dislocation loops as well. Hence, it becomes necessary to form a high density of small dislocation loops with very short misfit segments rather than a lower density of large dislocation loops with longer misfit segments to relieve the same amount of strain energy. This case is shown in the schematic of figure 7(c), where short MDs as part of dislocation loops (1) and planar stacking faults as part of trench defects (2) are confined to the nearby cap layer. The threading segments at the boundaries of these short in-plane defects then extend to the surface in high density and open to small V-pits, which in turn provide another means of strain relaxation. Given that some small V-pits are seen without visible threading defects beneath them, and they are in and of themselves as a possible strain relaxation route as we discussed in previous sections, this scenario (3) is also illustrated in figure 7(c). Jia et al. have shown that V-pits in QWs structures are a route for efficient current injection into the active region, which leads to an overall increase of the device efficiency [24]. In our microscopy study, we have shown the formation of small, randomly-distributed V-pits penetrating into the QW structures grown on partially relaxed porous InGaN pseudo-substrates and that the density of these small V-pits can be engineered by the porosity of the underlying template. Thus, the porosification of the pseudo-substrates not only allows control of the strain relaxation in the MQWs of the heterostructure but might also be a route to improve the device efficiency via V-pit engineering.

5. Conclusion

We have investigated the origins of small V-pits appearing in MQWs overgrown on non-porous and porous SL templates. Our previous work had indicated that porous SL templates lead to strain relaxation, and hence the appearance of a higher density of additional V-pits in QWs grown on such structures compared to those on non-porous templates was surprising. On the non-porous templates, we have shown that the small V-pits can arise from the intersections of either TDs or SMBs with the sample surface. Additional TDs arise when MDs glide from the top surface into the sample to relieve strain. These MDs often glide down into the SL itself. In comparison, SMBs arise when SFs form at an interface of the heterostructure during growth.

During overgrowth on the partially relaxed porous templates, the indium content of the MQWs increases with the degree of porosity, either because of a reduced compositional pulling effect or because of reduced thermal conductivity in the porous layer. Hence, although the template is relaxed, the driving force for relaxation in the higher In content MQWs may still be large. Furthermore, the porous structure prevents the glide of MDs into the SL and may inhibit the extension of the MDs due to strain and compositional inhomogeneities. Together, these effects provide an explanation for the observed additional small V-pits in MQWs overgrown on porosified templates. Finally, we note that the V-pit density can be managed via the extent of porosification in the SL template and that this may provide a useful control parameter for V-pit engineering to optimize current injection in longer wavelength LEDs.

Data availability

The data that support the findings of this study are available upon reasonable request from the authors. Readers may request permission from the repository to access the data by following this link: https://doi.org/10.17863/CAM.109091.

Acknowledgments

We would like to thank Innovate UK for the financial support within the Collaborative Research and Development scheme '*Porous InGaN for Red LEDs (PIRL)*' (Ref. 107470) and the EPSRC for support through Cambridge Royce facilities Grant EP/P024947/1 and Sir Henry Royce Institute—recurrent grant EP/R00661X/1. We acknowledge the use of the Thermo Fisher Spectra 300 TEM funded by EPSRC under Grant EP/R008779/1. We acknowledge the support of the technical staff Wolfson Electron Microscopy Suite at the University of Cambridge. This work was also supported by the Royal Academy of Engineering under the Chair in Emerging Technologies programme funded by the Department of Science, Innovation and Technology (DSIT).

Conflict of interest

Y Ji, M Frentrup, and S M Fairclough have no conflicts to disclose. Y Liu, T Zhu and R. A. Oliver have Patent US20230053213A1 pending.

Author Contributions

Yihong Ji: Investigation (equal), writing—original draft (lead).

Martin Frentrup: Investigation (equal), Supervision (equal), writing—review and editing (lead).

Simon M. Fairclough: Investigation (equal), writing—review and editing (equal).

Yingjun Liu: Conceptualization (equal), Funding Acquisition (equal).

Tongtong Zhu: Conceptualization (equal), writing—review and editing (equal), Funding Acquisition (equal).

Rachel A Oliver: Conceptualization (equal), Funding Acquisition (lead), Investigation (equal), Supervision (equal), writing—review and editing (lead).

ORCID iDs

Yihong Ji https://orcid.org/0009-0000-5147-3447
Simon M Fairclough https://orcid.org/0000-0003-3781-8212
Rachel A Oliver https://orcid.org/0000-0003-0029-3993

References

[1] Wierer J J and Tansu N 2019 III-nitride micro-LEDs for efficient emissive displays *Laser Photon. Rev.* **13** 1900141
[2] Lu Z, Zhang K, Zhuang J, Lin J, Lu Z, Jiang Z, Lu Z, Chen Y and Guo W 2023 Recent progress of InGaN-based red light emitting diodes *Micro Nanostruct.* **183** 207669
[3] Wang Z, Zhu S, Shan X, Yuan Z, Cui X and Tian P 2021 Full-color micro-LED display based on a single chip with two types of InGaN/GaN MQWs *Opt. Lett.* **46** 4358
[4] Li P *et al* 2022 Demonstration of ultra-small 5 × 5 μ m2607 nm InGaN amber micro-light-emitting diodes with an external quantum efficiency over 2% *Appl. Phys. Lett.* **120** 041102
[5] Liu L, Feng Q, Zhang Y, Zhu X, Chen L and Xiong Z 2023 Efficiency enhancement mechanism of piezoelectric effect in long wavelength InGaN-based LED *Phys. Chem. Chem. Phys.* **25** 27774–82
[6] Zhou S, Wan Z, Lei Y, Tang B, Tao G, Du P and Zhao X 2022 InGaN quantum well with gradually varying indium content for high-efficiency GaN-based green light-emitting diodes *Opt. Lett.* **47** 1291
[7] Ben Y, Liang F, Zhao D, Yang J, Chen P and Liu Z 2022 The direct evidence of the composition pulling effect and its role in InGaN multiple quantum wells *J. Mater. Res. Technol.* **21** 2228–37
[8] Lottigier P, Di Paola D M, Alexander D T L, Weatherley T F K, Sáenz de Santa María Modroño P, Chen D, Jacopin G, Carlin J F, Butté R and Grandjean N 2023 Investigation of the impact of point defects in InGaN/GaN quantum wells with high dislocation densities *Nanomaterials* **13** 2569
[9] Keller S, Pasayat S S, Gupta C, DenBaars S P, Nakamura S and Mishra U K 2021 Patterned III-nitrides on porous GaN: extending elastic relaxation from the nano- to the micrometer scale *Phys. Status Solidi* **15** 2100234
[10] Pasayat S S, Gupta C, Wang Y, DenBaars S P, Nakamura S, Keller S and Mishra U K 2020 Compliant micron-sized patterned ingan pseudo-substrates utilizing porous GaN *Materials* **13** 213
[11] Pasayat S S *et al* 2020 Color-tunable < 10 μ m square InGaN micro-LEDs on compliant GaN-on-porous-GaN pseudo-substrates *Appl. Phys. Lett.* **117** 061105
[12] Ji Y, Frentrup M, Zhang X, Pongrácz J, Fairclough S M, Liu Y, Zhu T and Oliver R A 2023 Porous pseudo-substrates for InGaN quantum well growth: morphology, structure, and strain relaxation *J. Appl. Phys.* **134**
[13] Costa P M F J, Datta R, Kappers M J, Vickers M E, Humphreys C J, Graham D M, Dawson P, Godfrey M J, Thrush E J and Mullins J T 2006 Misfit dislocations in In-rich InGaN/GaN quantum well structures *Phys. Status Solidi* a **203** 1729–32
[14] O'Hanlon T J, Massabuau F C P, Bao A, Kappers M J and Oliver R A 2021 Directly correlated microscopy of trench defects in InGaN quantum wells *Ultramicroscopy* **231** 113255

[15] Holec D, Costa P M F J, Kappers M J and Humphreys C J 2007 Critical thickness calculations for InGaN/GaN *J. Cryst. Growth* **303** 314–7
[16] El-Ella H A R, Rol F, Collins D P, Kappers M J, Taylor R A, Hu E L and Oliver R A 2011 InGaN super-lattice growth for fabrication of quantum dot containing microdisks *J. Cryst. Growth* **321** 113–9
[17] Stampfl C and Van De Walle C G 1998 Energetics and electronic structure of stacking faults in AlN, GaN, and InN *Phys. Rev.* B **57** R15052–R15055
[18] Massabuau F C P, Sahonta S L, Trinh-Xuan L, Rhode S, Puchtler T J, Kappers M J, Humphreys C J and Oliver R A 2012 Morphological, structural, and emission characterization of trench defects in InGaN/GaN quantum well structures *Appl. Phys. Lett.* **101** 212107
[19] Williams D B and Barry C 2009 *Transmission Electron Microscopy: A Textbook for Materials Science* (Springer)
[20] Massabuau F C P, Griffin P H, Springbett H P, Liu Y, Kumar R V, Zhu T and Oliver R A 2020 Dislocations as channels for the fabrication of sub-surface porous GaN by electrochemical etching *APL Mater.* **8** 8–13
[21] Even A, Laval G, Ledoux O, Ferret P, Sotta D, Guiot E, Levy F, Robin I C and Dussaigne A 2017 Enhanced in incorporation in full InGaN heterostructure grown on relaxed InGaN pseudo-substrate *Appl. Phys. Lett.* **110** 262103
[22] Spiridon B F, Griffin P H, Jarman J C, Liu Y, Zhu T, De Luca A, Oliver R A and Udrea F 2018 On-chip thermal insulation using porous GaN *Proceedings* **2** 776
[23] Surender S, Prabakaran K, Loganathan R, Pradeep S, Singh S and Baskar K 2017 Effect of growth temperature on InGaN/GaN heterostructures grown by MOCVD *J. Cryst. Growth* **468** 249–51
[24] Jia C, Hu X, Wang Q and Liang Z 2021 The effect of nanometer-scale V-pit layer on the carrier recombination mechanisms and efficiency Droop of GaN-based green light-emitting diodes *Phys. Status Solidi* a **218** 2100070